Access of energetic particles to Titan's exobase: A study of Cassini's T9 flyby

L.H. Regoli [a,b,c,*], E. Roussos [c], M. Feyerabend [d,e], G.H. Jones [a,b], N. Krupp [c], A.J. Coates [a,b], S. Simon [e], U. Motschmann [f], M.K. Dougherty [g]

[a] Mullard Space Science Laboratory, University College London Holmbury St. Mary, UK
[b] Centre for Planetary Sciences at UCL/Birkbeck, London, UK
[c] Max Planck Institute for Solar System Research, Göttingen, Germany
[d] Institute of Geophysics and Meteorology, University of Cologne, Germany
[e] Earth and Atmospheric Sciences, Georgia Tech, Atlanta, USA
[f] Institut für Theoretische Physik, Technische Universität Braunschweig, Germany
[g] Blackett Laboratory, Imperial College London, UK

ARTICLE INFO

ABSTRACT

We study how the local electromagnetic disturbances introduced by Titan affect the ionization rates of the atmosphere. For this, we model the precipitation of energetic particles, specifically hydrogen and oxygen ions with energies between 1 keV and 1 MeV, into Titan's exobase for the specific magnetospheric configuration of the T9 flyby. For the study, a particle tracing software package is used which consists of an integration of the single particle Lorentz force equation using a 4th order Runge–Kutta numerical method. For the electromagnetic disturbances, the output of the A.I.K.E.F. hybrid code (kinetic ions, fluid electrons) is used, allowing the possibility of analyzing the disturbances and asymmetries in the access of energetic particles originated by their large gyroradii. By combining these methods, 2D maps showing the access of each set of particles were produced. We show that the access of different particles is largely dominated by their gyroradii, with the complexity of the maps increasing with decreasing gyroradius, due to the larger effect that local disturbances introduced by the presence of the moon have in the trajectory of the particles with lower energies. We also show that for particles with gyroradii much larger than the moon's radius, simpler descriptions of the electromagnetic environment can reproduce similar results to those obtained when using the full hybrid simulation description, with simple north–south fields being sufficient to reproduce the hybrid code results for O^+ ions with energies larger than 10 keV but not enough to reproduce those for H^+ ions at any of the energies covered in the present study. Finally, by combining the maps created with upstream plasma flow measurements by the MIMI/CHEMS instrument, we are able to estimate normalized fluxes arriving at different selected positions of the moon's exobase. We then use these fluxes to calculate energy deposition and non-dissociative N_2 ionization rates for precipitating O^+ and H^+ ions and find differences in the ion production rates of up to almost 80% at the selected positions. All these results combined show that the electromagnetic field disturbances present in the vicinity of Titan significantly affect the contribution of energetic ions to local ionization profiles.

1. Introduction

With a radius of 2575 km, Titan is Saturn's largest moon and the second largest moon in the Solar System after Jupiter's Ganymede. Unlike Ganymede, Titan does not possess an internal magnetic field (Wei et al., 2010; Backes et al., 2005) but it is the only moon in the solar system known to have a dense atmosphere, with a surface pressure of 1.5 bar (Fulchignoni et al., 2005). The upper layers of the complex atmosphere are constantly ionized by different energy sources creating a complex ionosphere with different peaks that has been studied by several instruments on-board Cassini, both remotely and in situ. Additionally, chemical reactions may also be induced by the precipitation of energetic particles (Vuitton et al., 2007; Krasnopolsky, 2009).

* Corresponding author at: Max Planck Institute for Solar System Research, Göttingen, Germany.
E-mail address: regoli@mps.mpg.de (L.H. Regoli).

Titan's ionosphere has a complex vertical structure with different ionization sources like solar EUV radiation, precipitating energetic plasma from Saturn's magnetosphere, meteorites and galactic cosmic rays (Galand et al., 2010; Gronoff et al., 2009). The relative importance of these ionization sources is different for the dayside and the nightside of the moon (Cravens et al., 2009a). Whereas on the dayside solar radiation is the main ionization source (Galand et al., 2006; Ågren et al., 2009; Cui et al., 2009a), on the nightside impact ionization from incoming magnetospheric plasma, especially from electrons, becomes dominant (Galand et al., 2010; Richard et al., 2015). Additionally at the nightside, transport of ions coming from the dayside by horizontal winds has been shown to play an important role as well (Cui et al., 2009b).

The main ionospheric peak, created by the incoming solar radiation, is located at approximately 1200 km. Below that altitude different peaks are located that present significant changes in magnitude between different flybys (Kliore et al., 2008). The production of these peaks has been attributed to different ionization sources with López-Moreno et al. (2008) suggesting that galactic cosmic rays could be responsible for ionization at altitudes around 65 km, Molina-Cuberos et al. (2001) suggesting meteoritic ablation as the source for the mid-altitude peaks near 700 km and the impinging magnetospheric plasma being suggested as the responsible for the peaks at higher altitudes. Cravens et al. (2008) studied the energy deposition from H^+ and O^+ ions for energies above 30 keV as measured by the Cassini MIMI instrument and, by estimating ionization rates, suggested that the precipitation of those ions could be related to the formation of the density peaks observed between 500 km and 900 km.

These results are in agreement with more recent results from Snowden and Yelle (2014), who calculated energy deposition rates for thermal and energetic O^+ and H^+ ions while studying the thermal structure of the upper atmosphere. They found that while the peak deposition rate for thermal O^+ ions occurs at approximately 1100 km altitude for bi-modal populations and 1075 km altitude for plasma sheet populations (both classifications according to Rymer et al., 2009), energetic ions (with energies larger than 10 keV) deposit their energy below 1000 km.

More recently, Sillanpää and Johnson (2015) studied the influence of ion-neutral collisions, calculating energy deposition rates at the exobase using a hybrid code with different considerations in terms of types of interactions. There, they showed that the ion-neutral collisions greatly reduce the energy deposited in the upper atmosphere.

Titan is located at a mean distance of 20.2 Saturn radii (R_S) from the planet (1 R_S=60,268 km), placing it very close to the magnetopause stand-off distance, that Achilleos et al. (2008) described with a bi-modal distribution with peaks at 22 and 27 R_S (depending on the solar wind dynamic pressure) based on a magnetopause model by Arridge et al. (2006) and observations from Cassini. This locates Titan most of the time in the outer Saturnian magnetosphere where it has been observed for most of the dedicated flybys, even though it can be located both in the magnetosheath (observed three times during the first ten years of the Cassini mission, Bertucci et al., 2008; Wei et al., 2011 and Edberg et al., 2013) and in the unshocked solar wind (observed once, Bertucci et al., 2015).

In addition to these variabilities, even when Titan is completely immersed in the outer magnetosphere of Saturn, the surrounding environment can be highly variable in time scales that can go from minutes to hours since the moon can be located above, below or inside Saturn's magnetodisk that, as described in Arridge et al. (2008), has a bowl shape that is dependent on the season and the solar wind conditions.

Due to the fast rotation of the planet (Saturn completes a rotation around its axis in approximately 10 h 34 m, Read et al.,

2009) the heavier species of the plasma tend to be confined close to the equator but, as described in Arridge et al. (2011), due to the ambipolar electric fields that arise from the charge separation due to the high mobility of the electrons, lighter ion species such as H^+ tend to be located on a wider region around the equator than heavier species like O^+. This creates a latitude-dependent difference in the plasma composition that introduces a further variability to the plasma environment on which Titan can be immersed at any given time.

All of this together determine the structure of Titan's magnetospheric interaction region, which typically differs from that of a moon in a north–south magnetic field configuration (Arridge et al., 2011) and can be encountered immersed in a magnetospheric plasma flow with directions that differ from purely azimuthal corotation. The resulting structure has also implications on how particles can access the exosphere and deposit their energy into lower atmospheric layers and because of this variability, it becomes necessary to study these phenomena on a case-by-case basis. Apart from the obvious variability to be expected due to the different incoming fluxes that can significantly change from one flyby to the other (e.g. Garnier et al., 2010), the specific electromagnetic field configuration for each flyby will guide particles with different gyroradii in a different way, accessing the atmosphere with a different latitude- and longitude-dependent probability.

In this paper we focus on the effect that the uneven access of energetic particles into Titan's atmosphere due to local electromagnetic field disturbances may have in the structure of the ionosphere. For this we study the trajectories of H^+ and O^+ ions with energies from 1 keV up to 1 MeV by means of a particle tracing software package. Charged particle tracing has been successfully used to study the interaction of magnetospheric plasma with solar system bodies in many occasions with some recent applications specifically for the Saturnian system (e.g. Wulms et al., 2010; Kotova et al., 2015).

In general, the access of particles to the atmosphere will be determined by the local electromagnetic topology, which for Titan is highly variable as described above. For this study we selected the T9 flyby which occurred in conditions of non-azimuthal flow and magnetic field offset from the north–south direction, better illustrating the effect that the disturbances might have in the trajectories of charged particles. For the specific electromagnetic field configuration present during the flyby, reproduced by the A.I. K.E.F. (Adaptive-Ion-Kinetic-Electron-Fluid) hybrid code (Müller et al., 2011; Feyerabend et al., 2015 on this issue), we create 2D projections of Titan's exobase showing the access of particles and combining these maps with the fluxes measured by the Cassini MIMI instrument, we are able to estimate the incoming ion fluxes for different positions around the moon.

Finally, these fluxes are used to make estimations of energy deposition and ionization rates at different positions around the moon in order to quantify the effect that the asymmetries in the access of particles have in the global ionospheric structure.

1.1. The flyby

On 26 December 2005, Cassini flew at a distance of 10,411 km (4 R_T, closest approach (CA) at 18:59) from Titan in an equatorial trajectory especially interesting for studying the magnetospheric configuration of the moon's magnetic tail. The trajectory is shown in the Titan Interaction System (TIIS, Neubauer et al., 2006) coordinate frame in Fig. 1 where projections on the three different planes (XY, YZ and XZ) are represented.

The magnetospheric environment during the flyby was described by Rymer et al. (2009), based on electron spectra obtained by the Cassini CAPS/ELS instrument, as plasma sheet-like,
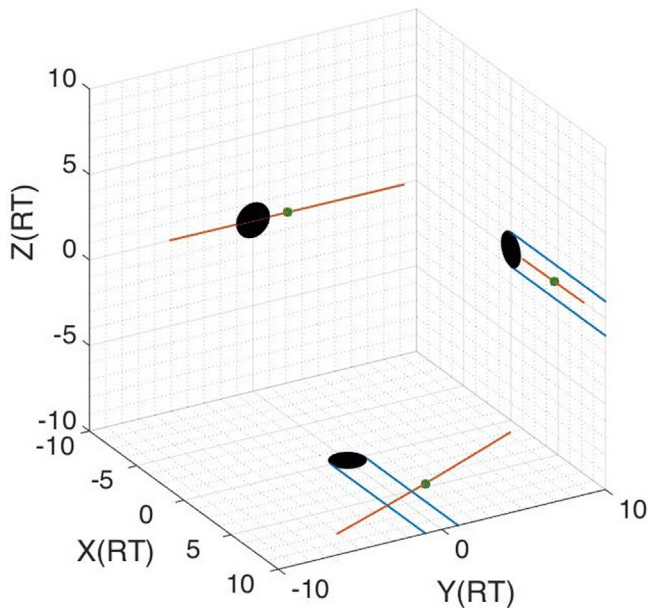
Fig. 1. Cassini trajectory during the T9 flyby shown in the TIIS coordinate frame. The *X*-axis points in the direction of ideal corotation, the *Y*-axis points towards Saturn and the *Z*-axis points northwards. The red line represents the spacecraft trajectory with the green point in the middle representing the moment of closest approach. The ideal corotation tail is represented by the two parallel blue lines. (For interpretation of the references to color in this figure caption, the reader is referred to the web version of this paper.)

with the moon located below the current sheet (Sittler et al., 2010). Many different analyses of the data provided by different instruments on-board the spacecraft as well as modeling of the magnetospheric environment using different techniques were performed for this specific flyby (Szego et al., 2007; Coates et al., 2007; Bertucci et al., 2007; Sittler et al., 2010).

Among the interesting features that were studied Coates et al. (2012), using data from the Cassini CAPS/ELS instrument, reported the existence of a split signature to the tail with presence of ionospheric photoelectrons, suggesting a magnetic connection of the tail with the sunlit part of the moon. This same tail structure, with two lobes and a central current sheet, was observed by the magnetometer (MAG) instrument, as reported by Bertucci et al. (2007). There, they suggested that this complex structure could be caused by the connection of each lobe to the dayside and the nightside respectively or, alternatively, to perturbations occurring in the upstream conditions, even though this last interpretation seems to be contradicted by the observation of the same split structure during subsequent tail flybys (Coates et al., 2012). Szego et al. (2007) interpreted the first structure as Titan's mantle and the second one as the moon's wake, with a region in between where ambient plasma was observed.

Similar observations were made using the Cassini Radio and Plasma Wave Science (RPWS) instrument as reported by Modolo et al. (2007). Apart from the asymmetry of the wake, they also reported a displacement of the ideal corotation wake, something that has been reproduced by different models and analyses, with Bertucci et al. (2007) setting the displacement at an angle of 36°. Coates et al. (2012), based on Cassini CAPS data analysis, interpret the plasma flow as having a southward component while Szego et al. (2007) concluded that the deflection should be larger than 40°. For the simulations presented in this paper, a deflection of 34°, as used on a hybrid simulation by Simon et al. (2007) in order to reproduce the observed MAG data, is assumed.

2. Model and simulations

In order to map the access of energetic ions to Titan's exobase, a particle tracer is used to follow the ion trajectories in the system. As energetic ions carry low current density, their impact on the electromagnetic field topology is negligible and a simple tracing algorithm works as a reasonable approximation. Still, the background electromagnetic environment upon which ions will be propagated needs to be defined.

In the following subsections, the basics of the tracing code as well as the electromagnetic field description used to obtain the plots presented in the results section are explained.

2.1. Tracing code

The basic equation of motion for charged particles in an electromagnetic field is the Lorentz force, given by Eq. (1), where $\overline{v}$ is the particle's velocity, $\overline{E}$ the electric field, $\overline{B}$ the magnetic field, q the particle's charge, m the particle's mass and γ the relativistic Lorentz factor.

$$\frac{d(\gamma \cdot m \cdot \overline{v})}{dt} = q \cdot (\overline{E} + \overline{v} \times \overline{B}) \tag{1}$$

In order to study the access of particles to Titan's exobase, we integrate the equation of motion in a particular magnetospheric configuration using a fourth order Runge–Kutta method.

The integration can be forwards or backwards in time, depending on the chosen approach. Forward integration can be useful for studying how a system with some given initial conditions evolves in time, whereas backward integration is a more sensible approach when one wants to study how the system gets to a specific final position in phase space (Marchand, 2010).

Since we are interested in the access of particles to the exobase, the problem reduces to studying how the evolution of particles occurs to finally reach a specific position in space. By using the backward tracing approach, a great amount of computational time is saved, avoiding the calculation of trajectories of billions of particles that would never reach the exobase (and thus would be of no interest for the present study) and would still be required if forward tracing were used. Additionally, backward tracing has the advantage that, given that the simulations are non-collisional, no statistical sampling errors are introduced, leaving the approximate nature of the electromagnetic fields and integration methods used as the only sources of error (Marchand, 2010).

Thus, the approach used here to estimate the access of particles is the use of backtracing of different particles with different physical characteristics (energy, starting polar and azimuthal angles), all of them starting at the same altitude above the moon's surface but at different positions defined by latitude and longitude angles. The starting altitude is that of the exobase, taken for this study as located at an altitude of 1450 km above the surface (Yelle et al., 2014). The choice of this altitude and the impact that moving this boundary has on the results presented on this paper are analyzed in Appendix A.

Notice that for each starting point, depending on the characteristics of the particle being simulated (e.g. polar angle, energy, etc.), the particle may or may not collide with the moon. This is illustrated in Fig. 2, where the trajectories of four hydrogen ions with different energies starting at the same initial position can either collide with the moon or escape the system, basically depending on the starting velocity vector and gyroradius.

As initial positions for the simulations, 10,800 equally spaced points around the moon were chosen, covering a range in latitude values from −90° to +90° and in longitude from 0° to 360°, both with linear steps of 1°. The coordinate system being used is the TIIS, where 0° latitude is defined as the moon's equatorial plane, 0°
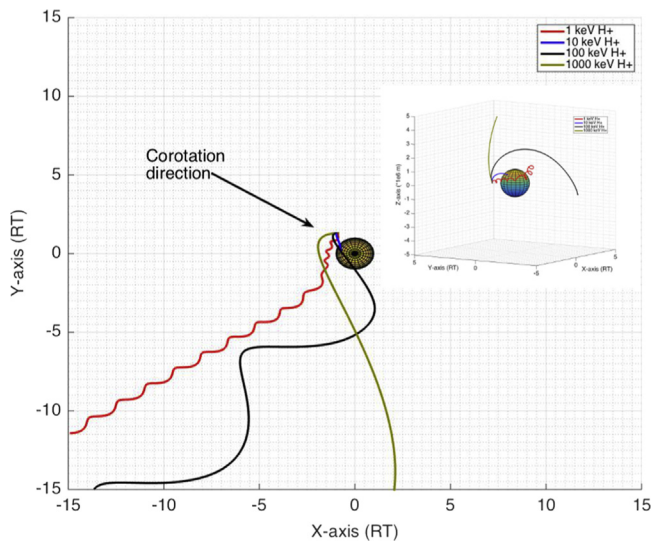
Fig. 2. Trajectories of four different H^+ ions starting at the same initial position. All the ions were simulated with the same starting polar and azimuthal angles, the only difference being their starting energy. The difference in gyroradius that is induced by this difference in starting energies leads to completely different trajectories, with 10 keV ion colliding with the moon soon after starting the simulation while the others finally escape the interaction region.

Fig. 3. Equirectangular projection of Titan's exobase showing the access of 1 keV electrons for an ideal north–south field configuration. The white vertical line indicates the position of the ram direction while the black vertical line indicates the position of the tail. Due to the uniform nature of the magnetic field configuration used and the lack of parallel velocity of the propagated particles, a large depletion in the access of particles is observed on the tail of the moon. Small areas on the tail where particles can access are present since the lower boundary of the simulation is taken 50 km below the defined exobase (see text for further explanation). (For interpretation of the references to color in the text, the reader is referred to the web version of this paper.)

longitude corresponds to the ideal corotation direction (aligned with the positive *X*-axis) and 90° (aligned with the positive *Y*-axis) corresponds to the Saturn direction.

For each of the starting points described, 6480 particles were simulated, each of them with a different combination of polar and azimuthal angles, each parameter varying from 0° to 180° and from 0° to 360° and with linear steps of 2° and 5° correspondingly.

All of the above give a total number of particles of roughly 70 million being simulated for each energy and for each species. For the present study, two different species were included, namely hydrogen (H^+) and oxygen (O^+) ions. In terms of energy, for each species a range going from 1 keV to 1 MeV was covered.

2.2. Code validation

In order to determine whether the integrating process yields the right results or not, simple runs simulating particles with pitch angles of 90° (i.e. no parallel velocity component) assuming a vertical north–south (along the *Z*-axis on a TIIS coordinates system) magnetic field configuration with azimuthal corotation were performed and the corresponding maps showing the access of particles were produced, yielding the expected results as shown in Fig. 3 , where a depletion of particles on the regions close to the magnetic tail can be observed, whereas full access is present for the rest of the local positions around the moon.

The map represents an equirectangular projection in Saturn-centered coordinates of Titan's exobase with the *X*-axis representing the longitude angle and the *Y*-axis representing the latitude angle. The color code represents the percentage of simulated particles that are able to escape the moon's environment during the backward tracing, which is the same as the regions that particles with the given characteristics would be able to reach in the moon's exobase in normal conditions (or forward tracing). The white line indicates the position of the ideal corotation direction (90° longitude) and the black line indicates the position of the tail (270° longitude). A depletion centered at the position of the magnetic tail is clearly visible, something expected for a plasma flow in a north–south magnetic field configuration. The small regions with access close to the poles in the position of the tail are present because, during the simulation, particles are allowed to
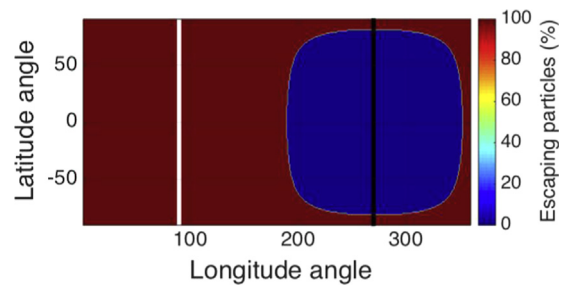
propagate downwards for a short distance (50 km) below the exobase and thus particles that start in the backward tracing at the exobase close to the poles are able to escape through that small region.

The idea of allowing the particles to propagate downwards is based on the selection of the boundary conditions for the simulations. Once the simulation starts, it is necessary to decide when to stop it. For this, two different boundary conditions need to be defined: (1) what happens when a particle hits the specified lower boundary and (2) when to stop the simulation assuming that the particle left the interaction region.

For the first one, since we are interested in the access of particles to the exobase without considering any propagation into a collisional environment, the boundary has to be located at (or close to) the exobase. In our simulations, particles are allowed to penetrate up to 50 km in order to avoid eliminating particles that could make a small incursion into lower altitudes (e.g. due to gyroradius effects) before departing from the moon. Thus, the inner boundary for the simulations shown in this paper is not exactly the starting point (exobase at 1450 km) but a hard limit of 1400 km. This boundary is still considered a collision-free environment with many authors using it as the position of the exobase (e.g. Ledvina et al., 2012; Wulms et al., 2010; Sittler et al., 2009). Since we are running single independent particle simulations, there is no need to avoid discontinuities in the densities so particles can be abruptly removed from the simulation without affecting the overall results. So as soon as a particle reaches an altitude of 1400 km above the surface it is removed from the simulation and assumed as lost.

For the second boundary, the condition that the particle being simulated reaches a position in space with undisturbed magnetic fields needs to be fulfilled. This means that the particle has to reach a position where the magnetic field is equal to the upstream field.

However, given that particles with large gyroradii could still return to the interaction region (Fig. 4), an additional condition is applied, which consists of letting the particle travel far from the moon and coming back after one gyration. If after this first gyration the particle does not collide with the moon but rather keeps drifting away from it, then it is finally assumed as escaped.

Validating computation parameters such as the integration step is not so straightforward. The approach taken was to save the initial and final velocity of the particles being simulated and taking the mean speed variation for each starting position (longitude/ latitude angle pairs). Even though variations are expected due to the presence of the electric field, these variations should not be
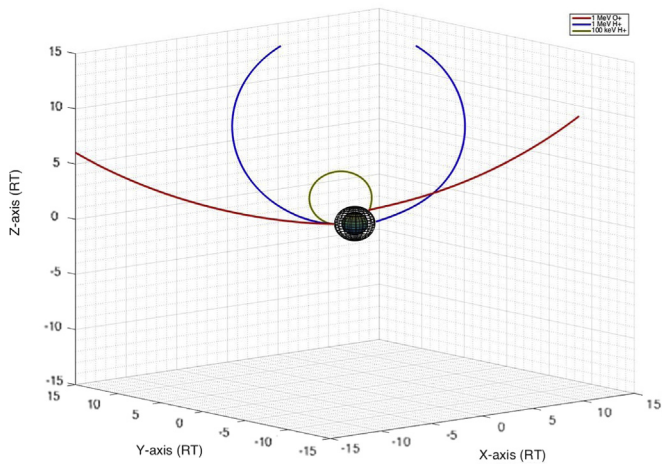
Fig. 4. Example of particles with gyroradii larger than the moon colliding after one gyration. All the three particles shown in the plot reached a region of undisturbed electromagnetic field upstream of the moon but, due to their large gyroradii, returned to the interaction region after one gyration and finally collided with the moon's exobase (shown as the black grid surrounding the moon in the center of the figure). Notice that the choice of the inner boundary (the black grid) could affect the access maps presented in the results section, with for instance the particle with the red trajectory possibly escaping the system if the boundary were set at a lower altitude. This effect is analyzed in Appendix A. (For interpretation of the references to color in this figure caption, the reader is referred to the web version of this paper.)

too large, given the fact that the electric field is mostly expected to be in a direction perpendicular to the magnetic field.

2.3. Electromagnetic fields

A number of different approaches have been used to study the electromagnetic configuration around Titan, including MHD (e.g. Ma et al., 2004), multi-fluid (Snowden et al., 2007), hybrid (e.g. Simon et al., 2007; Sillanpää, 2008; Lipatov et al., 2014), test particle (Luhmann, 1996), test particle/MHD (Ledvina et al., 2005; Tseng et al., 2008) and test-particle/hybrid (Wulms et al., 2010) simulations.

In this paper, the output generated for the T9 flyby by a hybrid code named A.I.K.E.F. (Müller et al., 2011) is used. In the model, ions are treated as individual particles while electrons are treated as a neutralizing fluid. Fig. 5 shows the equatorial magnetic field (as seen from above) for the specific conditions of the T9 flyby with the colors representing the magnitude.

In the hybrid code simulation, both the magnetic and electric fields are self-consistently calculated during the production of the output and these (static) values are used during our tracings. For our tracing, a snapshot of the calculated fields was used. Titan itself is treated as an absorbing obstacle, meaning that any ion macroparticle in the code that reaches the inner boundary is removed from the simulation.

For the ionosphere, three species were included, namely H_2^+, CH_4^+ and N_2^+ and the massloading of the plasma was simulated by photoionization. Since we are interested only in the magnetic field perturbations and not in the ion densities, this relatively simple approach is sufficient for our purposes.

The upstream parameters used during the production of the hybrid code output for the T9 flyby are summarized in Table 1. All the upstream parameters were kept constant during the simulation run (for more details refer to Feyerabend et al., 2015 on this issue).

Given the short time scale of the studies presented here, taking the fields as invariant during the tracing is a sensible assumption. Nevertheless, the hybrid code output for this study is provided self-consistently only within a cube of 15 Titan radii (1 $R_T = 2575$ km)
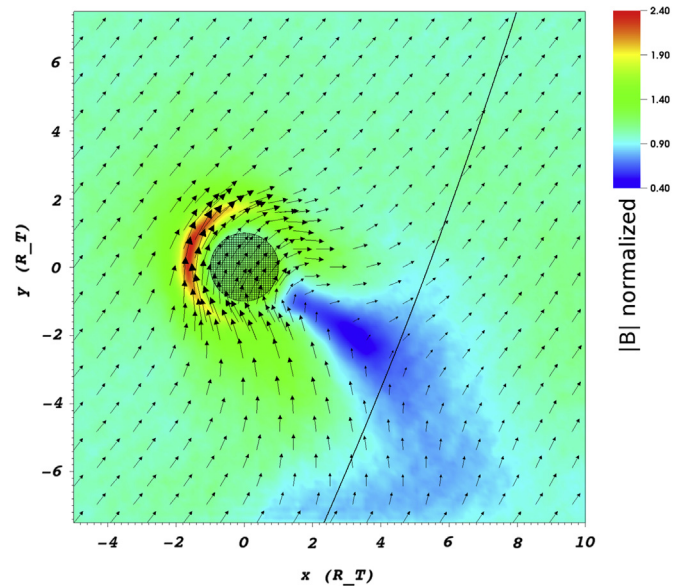

Fig. 5. Equatorial magnetic field in TIIS coordinates within a simulation box of 15 R_T side during the T9 flyby as calculated using the hybrid code A.I.K.E.F. The colors represent the magnitude of the magnetic field normalized to the upstream field magnitude (6.37 nT) and the black line shows Cassini's trajectory during the flyby. (For interpretation of the references to color in this figure caption, the reader is referred to the web version of this paper.)

Table 1
Upstream plasma parameters for the hybrid code output (Feyerabend et al., 2015 on this issue).

Parameter	Value
Saturn local time	3:00
Latitude of subsolar point	$-19.06°$
Upstream magnetic field vector	$(3.73, 4.7, -2.15)$ nT
Upstream magnetic field strength	6.37 nT
Number density of upstream O^+	0.2 cm^{-3}
Number density of upstream H^+	0.1 cm^{-3}
Upstream plasma bulk velocity	120 km/s
Alfvénic Mach number	2.22
O^+ gyroradius	1.21 R_T
H^+ gyroradius	0.08 R_T

side. This choice is based on the high computational times required for the hybrid code simulation. Even though the hybrid code simulation is run with an adaptive mesh with higher spatial resolution closer to the moon, the output used on this study has been re-sampled to a uniform grid with 280 sample points on each of the three directions, giving a resolution of 0.05 R_T.

Once the particles being traced leave the hybrid code cube, it becomes necessary to extend somehow the electromagnetic field model to continue with the tracing. Particles can leave the 15 R_T side cube either due to their large gyroradii or due to their motion along the field lines. In the first case, particles will make a relatively short excursion outside the cube whereas in the second case they will gyrate around the field line while traveling with a parallel velocity component to their mirror point and back. For this last case, a full magnetospheric model (e.g. Khurana et al., 2006) would be needed whereas for the former one a simpler approach can be used.

Whether particles need to be traced to their mirror points or not depends mainly on their equatorial displacement during half a bounce period. If this displacement is large enough so that the particle can be removed from the simulations once it leaves the interaction region, then a simple description can be adopted for the vicinity of the moon. This is indeed the case for all the particles
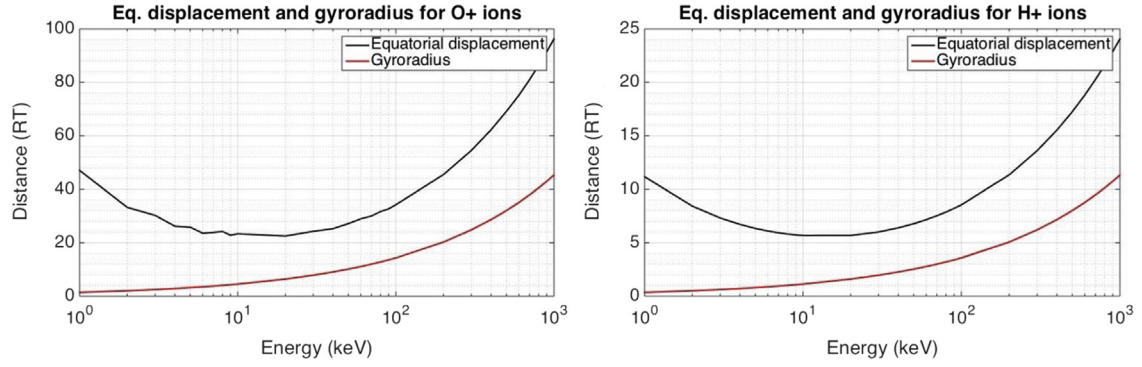
Fig. 6. Half-bounce averaged equatorial displacement and gyroradius for O^+ and H^+ ions at different energies.

Table 2
Equatorial displacement (ED) and gyroradius (R_G) for O^+ and H^+ ions with different energies.

E (keV)	ED O^+ (R_T)	R_G O^+ (R_T)	ED H^+ (R_T)	R_G H^+ (R_T)
1	47.02	1.43	11.17	0.36
5	25.83	3.20	6.35	0.80
10	23.36	4.53	5.68	1.13
50	27.16	10.13	6.78	2.53
100	34.25	14.33	8.55	3.58
500	69.13	32.04	17.25	8.01
1000	96.28	45.3	24.07	11.32

studied in this paper with the minimum expected equatorial displacement being at least 3.5 times larger than the particle's gyroradius. This can be observed in Fig. 6, where the equatorial displacement and corresponding gyroradius are plotted for H^+ and O^+ ions and for each energy level covered in this study. In both cases, a minimum is reached at an energy of 20 keV, where the displacement-to-gyroradius ratio is of 3.5, allowing the particle to drift away from the moon without colliding with it after returning to its vicinity. Table 2 presents the drifts for selected energies.

The drifts were calculated using the full magnetospheric model (Khurana et al., 2006) with 60% corotation by means of the method presented in Roederer (1967) considering pitch angles close to 90°. The calculation includes both a magnetic field-related drift and an electric field-related drift. The magnetic drift is calculated using Eq. (2), where m_0 is the particle's mass, c is the speed of light, q is the elementary charge, B_{eq} is the equatorial magnetic field at the L-shell where the calculation is being performed, γ is the relativistic Lorentz factor and I and S_b are line integrals related to the length of the magnetic field lines and are calculated using Eqs. (3) and (4) respectively.

$$v_m = \frac{m_0 \cdot c^2}{q \cdot B_{eq}} \cdot \frac{\gamma^2 - 1}{\gamma} \cdot \frac{\nabla I}{S_b} \tag{2}$$

$$I = \int_{-\lambda_m}^{\lambda_m} \left(1 - \frac{B(s)}{B_m} \right)^{1/2} ds \tag{3}$$

$$S_b = \int_{-\lambda_m}^{\lambda_m} \left(1 - \frac{B(s)}{B_m} \right)^{-1/2} ds \tag{4}$$

In both equations λ_m represents the latitude of the particle's mirror points, $B(s)$ is the magnetic field at the position where the numerical integral is being calculated and B_m is the magnetic field magnitude at the mirror points.

The electric drift is simply the $E \times B$ drift as calculated using

$$v_e = \frac{E \times B}{B^2} \tag{5}$$

For this reason, a simple extension of the hybrid code output is taken. This extension consists of taking the electromagnetic field values 5 R_T upstream of the moon, where the presence of the moon itself causes no distortion, and using them for every point outside the hybrid code cube. This approach significantly reduces the computation time when compared with other methods such as using full magnetospheric models and the values of the hybrid code output for the selected position are in good agreement with the readings from the MAG instrument on-board Cassini for the T9 flyby outside the interaction region as presented in Bertucci et al. (2007).

3. Results

In this section, maps showing the access of particles to Titan's exobase are presented and discussed. For reasons of space, only maps for four different energies for O^+ and H^+ ions are presented in order to show the variabilities that arise from the different gyroradii.

In addition to the mentioned maps, the influence that variations in the field configuration have in the access of particles is studied by comparing the maps obtained using three different models: (1) a uniform, north–south magnetic field, (2) a uniform, rotated, magnetic field with the upstream values from the hybrid code output and (3) the full hybrid code output which accounts for the draping of the lines close to the moon.

The results are presented in the form of equirectangular projections of Titan's exobase as shown in Fig. 3. The only difference between Fig. 3 and the maps presented in this section is the position of the white and black lines; whereas in the map presented in Fig. 3 those lines represented the ideal corotation and tail positions, in the ones presented here they represent the positions of the assumed direction of the upstream flow (ideal −34°, i.e. 146°) and of the magnetic tail (upstream flow +180°, i.e. 326°). In order to facilitate the comparison, whenever maps are presented together, the same color scale is used.

The access of particles obtained with the tracing in combination with energetic ion fluxes obtained from the Cassini MIMI instrument are then used to obtain estimated fluxes reaching specific positions of the moon. Finally, ionization rates curves for both O^+ and H^+ ions are presented.

3.1. Effect of different distortions in the access of particles

In this subsection, the effect that different distortions, such as the field rotation or the magnetic field lines draping, have in the
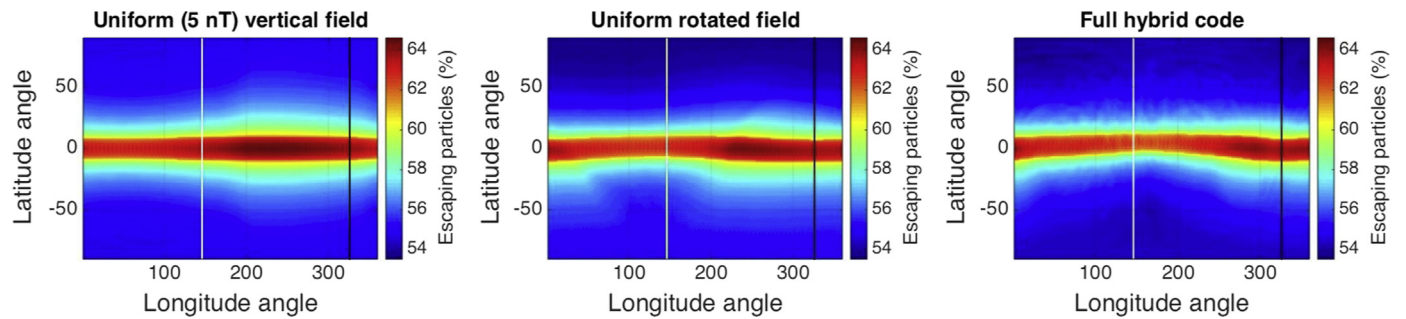
Fig. 7. Access of 10 keV O$^+$ ions to Titan's exobase for the case of a uniform vertical field (left), a rotated uniform field (center) and the full hybrid code output (right). The white vertical line indicates the position of the ram direction while the black vertical line indicates the position of the tail.
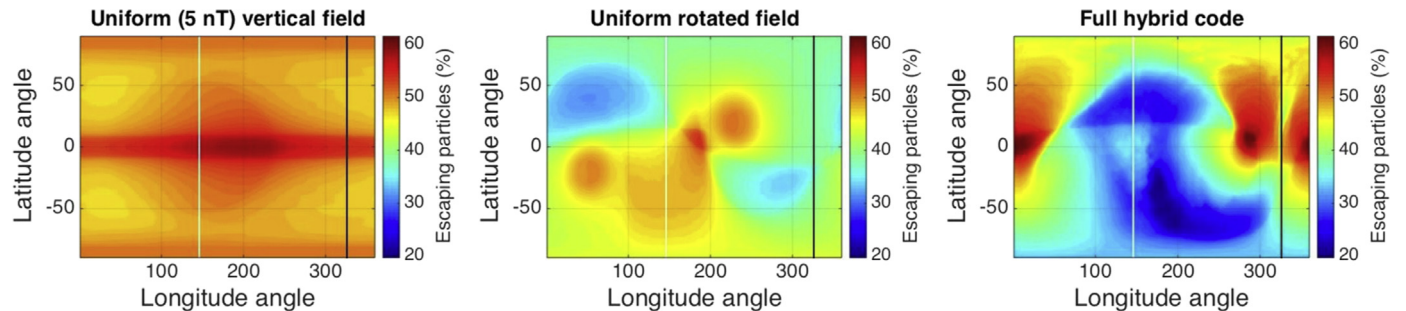

Fig. 8. Access of 10 keV H$^+$ ions to Titan's exobase for the case of a uniform vertical field (left), a rotated uniform field (center) and the full hybrid code output (right). The white vertical line indicates the position of the ram direction while the black vertical line indicates the position of the tail.

access of particles is discussed. For this, three simulations were run with a given set of particles: one with a uniform, vertical (north–south), magnetic field of magnitude 5 nT, one with a uniform electromagnetic field with components $(3.82, 4.69, -2.05)$ nT as taken from the hybrid code output at a position upstream of the moon (which already accounts for a strong Saturn-directed magnetic field component observed during the T9 flyby and that is present in the hybrid code output) and the full hybrid code model. From the three field configurations, only the last one (the hybrid code) accounts for the draping of the magnetic field lines around Titan.

Fig. 7 shows the results for the three aforementioned simulations for the case of 10 keV O$^+$ ions whereas Fig. 8 shows the results for the case of 10 keV H$^+$ ions.

These two cases illustrate, in a very clear way, how simpler descriptions of the fields are only sufficient for the simple access maps produced by particles with large gyroradii. While, for the case of the 10 keV O$^+$ ions (gyroradius of 1.8 R_T), a simple north–south description of the field satisfactorily reproduces the large scale structures of the map produced with the hybrid code output and the rotated field explains even most of the small scale features, for the 10 keV H$^+$ ions (gyroradius of 0.4 R_T) none of the simple field descriptions (the north–south and the rotated field configurations) yield results that are in agreement at any level with the full hybrid code description.

Overall, for all the energies included in this study, for H$^+$ ions only the hybrid code can create the maps showing all the large and small scale structures while for the O$^+$ ions, simpler field models are sufficient for energies larger than 10 keV. This is an effect of the shielding produced by the induced fields around Titan and has been described in other works like for instance Ledvina et al. (2005) and Shah et al. (2009). The importance of using realistic magnetic field descriptions was also pointed out by Wulms et al. (2010), where they concluded that it is the only way to understand the energetic neutral atoms (ENA) emissions detected by the Cassini INCA instrument.

3.2. Access of particles with the full hybrid code output

Fig. 9 shows the maps obtained using the full hybrid code output for O$^+$ with four different energy levels. From the color scale, it is evident how particles with higher energies have much higher access at every position around the moon, with the effect becoming less evident for particles with energy lower than 10 keV.

Additionally, a symmetry with respect to the equator is observable especially for the highest energies. This symmetry arises from the gyroradii of the particles that are in every case larger than the moon's radius (e.g. 5.3 R_T for 90° pitch angle O$^+$ ions at the equator with an energy of 100 keV and 15 R_T for the 1 MeV case). This causes that, in the close vicinity of the moon, particles travel with a trajectory very close to a straight line and thus the effect of the draping of the lines caused by the moon is almost negligible.

Finally, a wave-like shape is observed surrounding the symmetric feature mentioned in the previous paragraph, especially for the middle energies (e.g. 10 keV in Fig. 9). This effect is produced by the rotation of the field observed during the flyby. On a vertical magnetic field configuration, particles traveling along the magnetic field lines can reach the close vicinity of the moon either from the north or the south poles, creating an access pattern that is symmetric around the equator of the moon. If in contrast the magnetic field is rotated by a certain angle with respect to the equatorial plane, particles coming from the north will have more access at a certain longitude, while particles coming from the south will have more access at a completely different longitude, thus creating the observed structure.

Fig. 10 shows the maps obtained using the full hybrid code output for H$^+$ with four different energy levels. A similar effect like that observed with O$^+$ ions is present, with larger access in most regions of the exobase for higher energies. Similarly, the symmetry around the equator is also observable, even though the deviation from the symmetry arises with higher energies, showing for the 100 keV case an already noticeable wave-like shape and the symmetry completely absent for the 10 keV case.
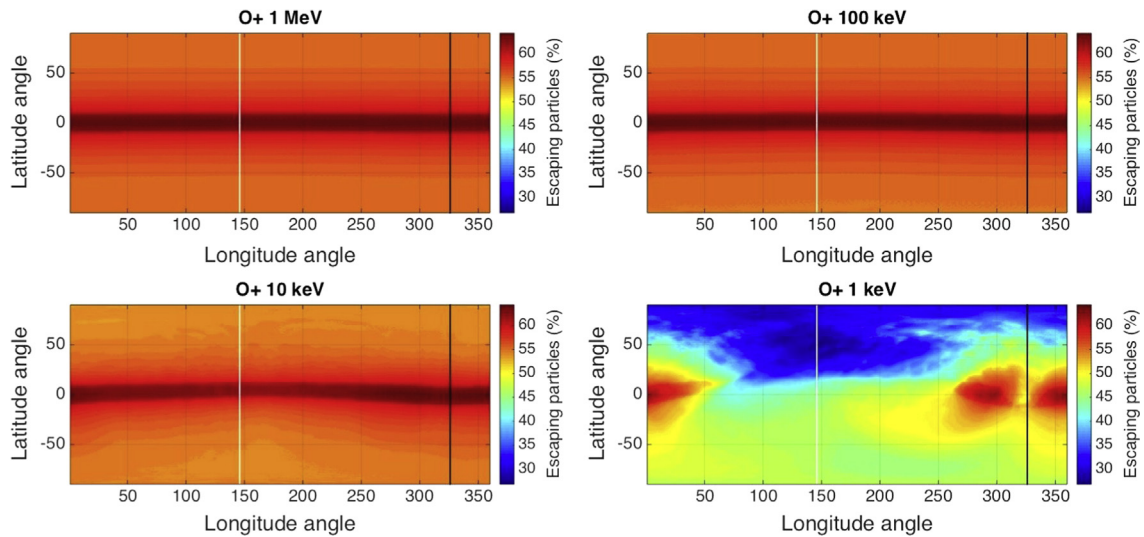
Fig. 9. Equirectangular projection of Titan's exobase showing the access of 1 MeV (top left), 100 keV (top right), 10 keV (bottom left) and 1 keV (bottom right) O^+ ions. The maps were created by propagating the particles on a background electromagnetic field generated by the A.I.K.E.F. hybrid code. The white vertical line indicates the position of the ram direction while the black vertical line indicates the position of the tail.
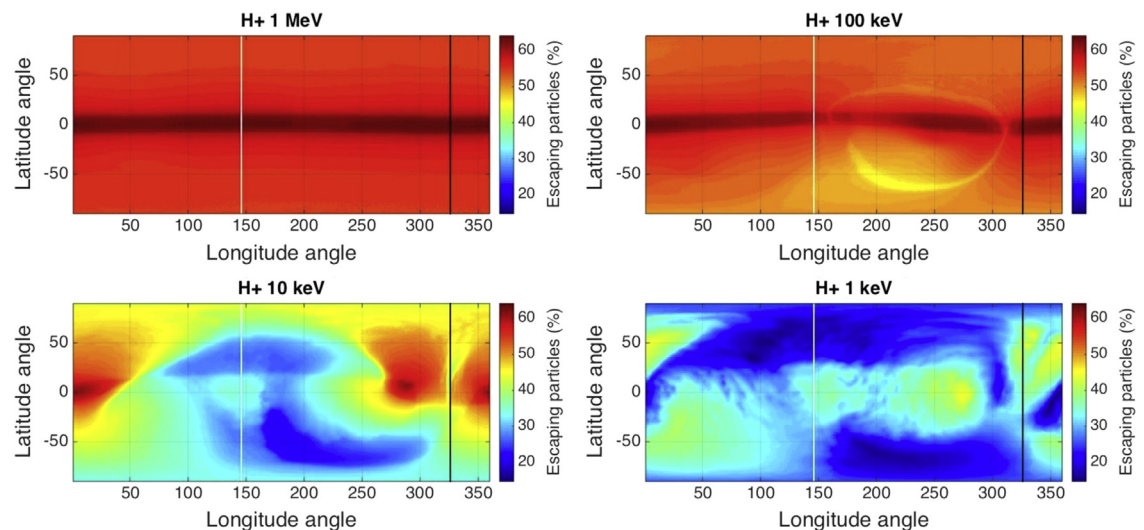

Fig. 10. Equirectangular projection of Titan's exobase showing the access of 1 MeV (left), 100 keV (center) and 10 keV (right) H^+ ions. The maps were created by propagating the particles on a background electromagnetic field generated by the A.I.K.E.F. hybrid code. The white vertical line indicates the position of the ram direction while the black vertical line indicates the position of the tail.

An interesting effect for both the O^+ and the H^+ case is that for the lower energies, the access of particles is larger for the region surrounding the magnetic tail than for the region from where the incoming plasma should be impinging the moon. Even though this has already been reported by other authors (e.g. Sillanpää et al., 2007), it seems counterintuitive and has its roots on the distortions of the electromagnetic fields introduced by the presence of Titan. To help visualize this, Fig. 11 shows the magnitude of the magnetic field at the exobase of Titan. In this projection it is evident that the magnetic field magnitude is much lower on the tail and much stronger at the ram direction. This helps shield the regions close to 150° while it leaves the regions close to the tail more unprotected due to the lower magnetic field magnitude. This basically affects particles with smaller gyroradii that tend to drift on curves of equal magnetic field and will thus tend to avoid the pile-up region present where the incoming plasma flow encounters the moon's ionosphere, while particles with larger gyroradii are able to access all the regions around the moon.

From the maps just presented it is possible to observe that the access of particles is not homogeneous around the moon, with some areas more accessible to specific particles with specific energies. This is easier to observe in Fig. 12, where the percentual access of O^+ and H^+ ions is plotted against the energy ranging from 1 keV to 1 MeV for four different selected positions around the moon (Table 3 and Fig. 11). The selection of the regions was based on visual inspection of the access maps presented above. The idea was to take regions with large and regions with small variations along the analyzed energy range.

In both plots, the first thing that can be seen is that the access is the largest in every case for the higher energies. In fact, for the four selected points at the exobase, the access steadily increases with energy until a steady level that varies with particle and position is achieved. This point is located at around 10 keV for the O^+ case for the four points and at around 300 keV for the H^+ case for three of the points with the Lat: 0°, Long: 0° case being stabilized at approximately 20 keV.
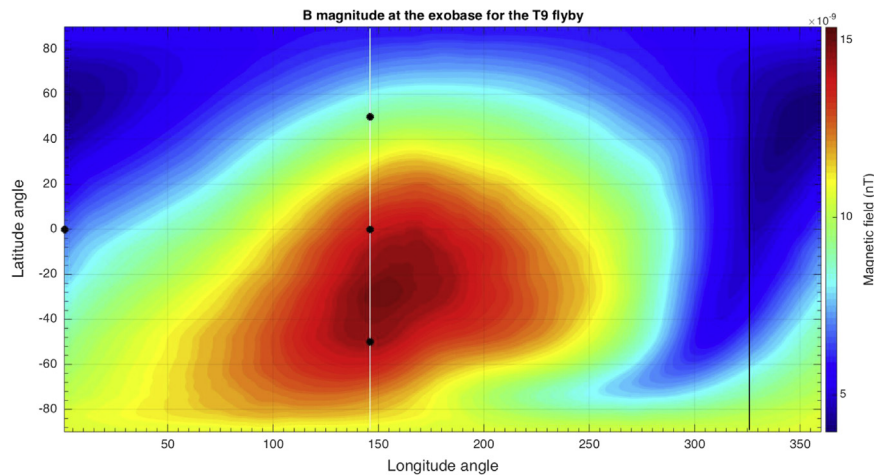
Fig. 11. Magnetic field magnitude for the T9 flyby at Titan's exobase as obtained from a hybrid code (A.I.K.E.F.) simulation. The white vertical line indicates the position of the ram direction while the black vertical line indicates the position of the tail. At the position of the ram direction, a pile up of the magnetic field lines enhances the magnetic field magnitude whereas a depletion of magnetic field lines can be observed on the tail, where the magnetic field magnitude is around 3 times smaller. This affects the access of particles with small gyroradii, allowing them to access regions close to the tail while preventing them to access regions close to the ram direction. The four black markers indicate the regions at which ionization rates are calculated (see later sections in the paper).
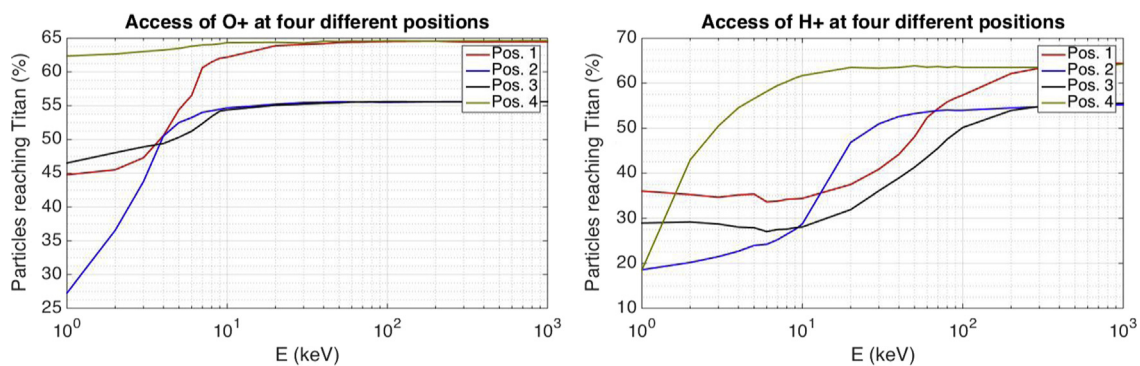

Fig. 12. Percentual access of O^+ and H^+ ions vs. Energy at four different locations in Titan's exobase.

Table 3
Selected positions at the exobase around the moon for ionization rates analysis.

Position	Latitude (deg)	Longitude (deg)
Position 1	0	146
Position 2	50	146
Position 3	−50	146
Position 4	0	0

Altogether, the two plots show how the access of particles is highly asymmetric all over the moon, with the asymmetry increasing with decreasing gyroradius. We interpret this asymmetry as one of the possible causes for the high variability observed in the ionospheric profiles obtained by in situ measurements by different instruments on-board Cassini (Cravens et al., 2009b and references therein). In the following subsection we derive energy deposition and ionization rates in order to explore this possibility.

3.3. Energy deposition and ionization rates

Since Titan was located below the current sheet during the T9 flyby, a strong Saturn-directed component was present in the magnetic field data. This is visible in Fig. 13 that shows the three magnetic field components as detected by the MAG instrument (Dougherty et al., 2004), as well as the magnitude in TIIS coordinates for a time span of three hours before and after CA. The solid line shows the point of closest approach and the dashed lines

indicate the region of undisturbed magnetic field used for the following analysis.

Fig. 14 shows the upstream fluxes of O^+ and H^+ detected by the MIMI/CHEMS instrument (Krimigis et al., 2004) before CA. The fluxes are average values obtained between 17:00 and 18:00 (dashed lines in Fig. 13) in order to avoid Titan's interaction region. The lines on the plot correspond to a Kappa distribution fit for the O^+ ions (red) and a combination of a power law and a Kappa distribution fit for the H^+ ions (blue). The Kappa distribution function used here (Eq. (6)) is the modified version presented by Dialynas et al. (2009). The energy coverage for CHEMS goes from 2.8 keV to 220 keV for H^+ and from 10.3 keV to 220 keV for O^+ but the spectra have been extended with the Kappa distribution fit until 1 MeV.

$$j = C \cdot E \left[E + kT(1 + \gamma_1) \right]^{-(1+\gamma_1)} \qquad (6)$$

By combining the O^+ and H^+ spectra shown in Fig. 12 with the upstream fluxes detected by the MIMI/CHEMS , we are able to estimate the normalized fluxes of different particles at given locations of the moon's exobase. These normalized fluxes are shown in Fig. 15 .

For both cases a difference between the upstream fluxes and the fluxes reaching the exobase is present, with the difference being the largest for the lower energies. This is again a result of the shielding effect being stronger for particles with smaller gyroradius and thus having a larger attenuating effect on the upstream fluxes for particles with lower energies than for those with higher energies.
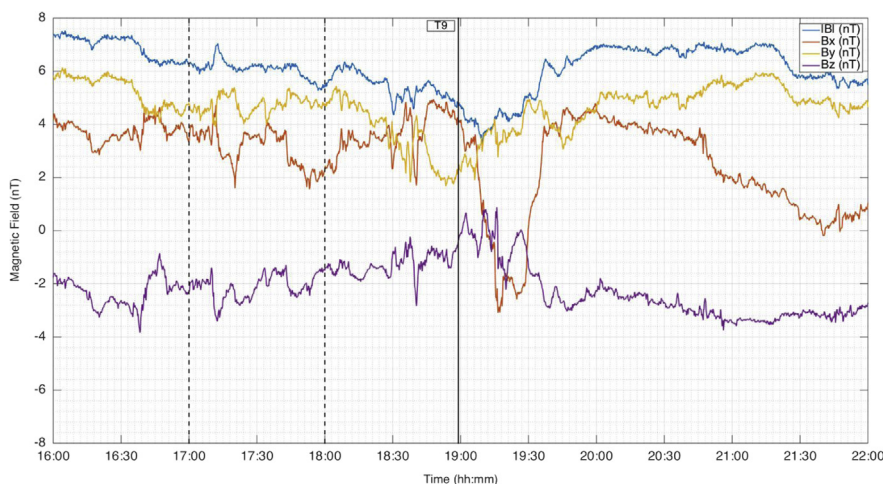
Fig. 13. Magnetic field data in TIIS coordinates three hours before and after closest approach (marked here with the solid black line in the middle of the plot) for T9. The dashed lines show the region of undisturbed magnetic field from which the ion data used in the analysis were taken. (For interpretation of the references to color in the text, the reader is referred to the web version of this paper.)
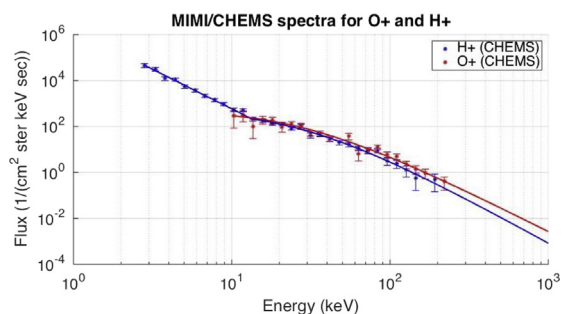

Fig. 14. MIMI/CHEMS spectra for O^+ and H^+ ions during the T9 flyby. The oxygen spectrum (red curve) was fitted with a Kappa distribution while the hydrogen spectrum (blue curve) was fitted with a power law for the lower energies and a Kappa distribution for the higher energies. Both spectra were extended with the fitted curve until 1 MeV. (For interpretation of the references to color in this figure caption, the reader is referred to the web version of this paper.)

Titan harbors a very complex atmosphere with high contents of different hydrocarbons that derive from two main components, namely molecular nitrogen (N_2) and methane (CH_4) (Bézard et al., 2014; Waite et al., 2005). The mole fractions vary with altitude from 98.4% N_2 and 1.31% CH_4 at 981 km to 96.6% N_2 and 3% CH_4 at 1151 km, as determined by Cui et al. (2009b) based on Cassini/INMS data obtained during 15 close Titan flybys. Given the dominance of molecular nitrogen with respect to the rest of the atmospheric constituents and since we are interested in the relative changes that the local disturbances of the electromagnetic fields introduce on the energy deposition and ionization rates, in the following analysis we only account for the precipitation of O^+ and H^+ ions into N_2.

For the calculation of the energy deposition by O^+ and H^+ ions into Titan's atmosphere, the altitude profile for the mass density of Titan's atmosphere from the engineering model presented in Yelle et al. (1997) was used. For the stopping powers for the simulated ions in molecular nitrogen (N_2), nuclear and electronic values from the SRIM software (Ziegler et al., 2010) were used.

SRIM (Stopping and Range of Ions in Matter) is a software package based on Monte Carlo simulations that calculates stopping powers for different ions in different compounds by combining experimental data with empirically derived equations. The advantage of using the SRIM software is that it provides stopping powers at a range of energies for which experimental data is not available, making it suitable for this specific case with accuracies around 4%, as reported in Ziegler et al. (2010).

The left panel in Fig. 16 shows the integrated ionization rates by O^+ ions with energies higher than 10 keV on the atmosphere. The figure shows that most of the ionization by energetic O^+ ions occur at an altitude of approximately 900 km above the moon's surface, where a production of roughly 4 ions/cm^3 is predicted.

To get an estimate of the differences in ionization rates at the selected positions around the moon, a weighted difference between the position where the maximum rate was observed and that where the minimum rate was observed was calculated. The difference is weighted according to the local magnitude of the ionization rate, normalized to the maximum value. This gives an estimate of the difference where the ionization rates are the highest and neglects altitudes at which the differences can be higher but the ionization rates are very low.

The curve showing the weighted difference is presented on the right panel of Fig. 16. A maximum difference between the peak ionization rates of 18% is calculated for this case. This difference was calculated between the position with highest ionization rate (position 4) and the one with the lowest ionization rate (position 3).

Fig. 17 shows the ionization rates for H^+ ions of the same energies as the O^+ ions shown in Fig. 16 ($E > 10$ keV). Since the N_2 stopping powers are smaller for precipitating H^+ than for precipitation O^+, hydrogen ions can penetrate deeper in the atmosphere, with the ionization rate peak located at approximately 820 km above the moon's surface. The peak magnitudes show a larger variations among different positions compared to the O^+ case, with a maximum of almost 4 ions/cm^3 for position 4 ($0°$ latitude and $0°$ longitude) and closer to 2 ions/cm^3 for position 3 ($-50°$ latitude and $146°$ longitude).

Also remarkable for the H^+ case is the higher magnitude of the weighted difference peak. Whereas for oxygen ions the peak was around 18%, for hydrogen the peak reaches almost 80%. In terms of altitudes and magnitudes, production rates for both the O^+ and the H^+ ions are in good agreement with the results derived for T5 by Cravens et al. (2008) where they present production rates for ions with energies above 30 keV, with only the ionization peak for H^2 occurring at slightly higher altitude in this study.

With this very simple ionization model, we are then able to estimate that the ionospheric density variations from magnetospheric ions precipitation due to the electromagnetic field disturbances observed during T9 would range from less than 20% to more than 75% at different positions around the moon. This means that if the differences observed in the ionospheric densities for the nightside of the moon (where the precipitating plasma plays an
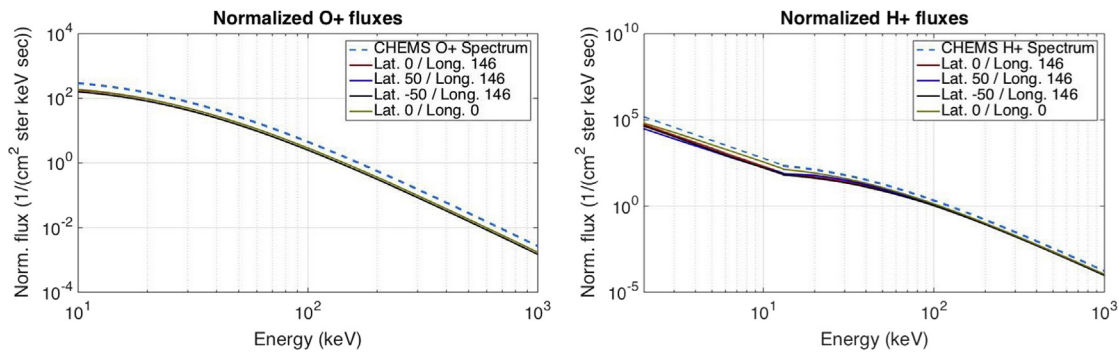
Fig. 15. Normalized flux vs. Energy for O^+ and H^+ ions at four different locations in Titan's exobase. These fluxes are used as an input for the ionization rates shown in Figs. 16 and 17.
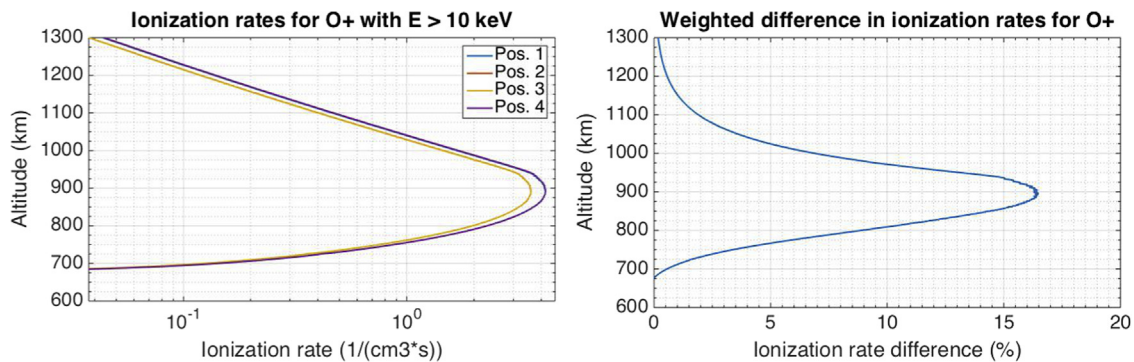

Fig. 16. Production rates from precipitating O^+ ions with energies higher than 10 keV (left panel) at four different positions around the moon and weighted difference between the positions with higher (position 4) and lower (position 3) rates.
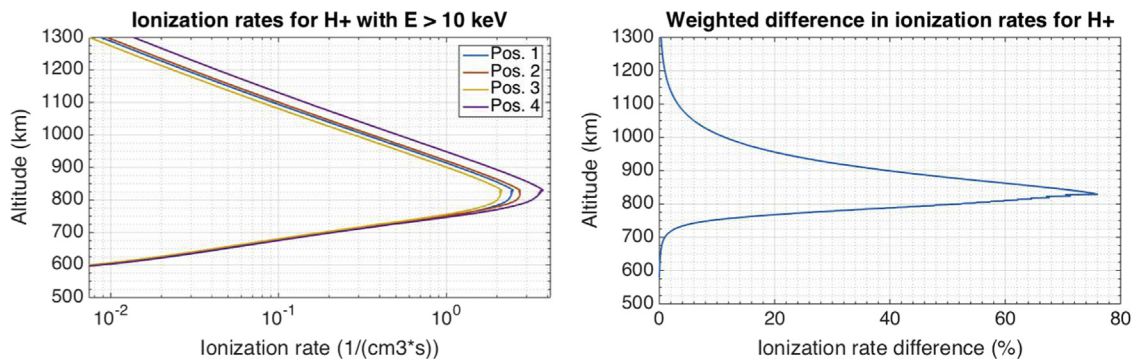

Fig. 17. Production rates from precipitating H^+ ions with energies higher than 10 keV (left panel) at four different positions around the moon and weighted difference between the positions with higher (position 4) and lower (position 3) rates.

important role on the ion production) are taken into account, part of them could be explained not just by the upstream plasma variations, but also by the difference in particle's access caused by the electromagnetic field disturbances present during the different flybys.

4. Summary

By means of particle tracing software and using three different magnetic field models, the effect that different disturbances present in the vicinity of Titan have in the access of particles to the exobase was studied. For this, three different simulations, namely one with a simple north–south field, a second using the upstream electromagnetic fields observed before and after the T9 flyby that includes the strong X_{TIIS} and Y_{TIIS} components and a third one with the full description provided by the A.I.K.E.F. hybrid code were compared for the same species and energies, showing that the

importance of having a full electromagnetic field description (such as the one provided by the hybrid code) increases with decreasing gyroradii. In this sense, it was shown that for particles with gyroradii larger than few R_T, a simple constant vertical field or an unperturbed field with a Saturnward component can produce very similar access maps than a full hybrid code description.

Then, by using the full hybrid code description of the electromagnetic fields specifically produced for the T9 flyby, we produced 2D projection maps of Titan's exobase showing the access of H^+ and O^+ ions of different energies. The results show how important the gyroradii of the particles is on determining the final location where they will reach the moon's exobase and hence deposit their energy.

It was shown how particles with large gyroradii (larger than the moon's diameter) produce simpler maps with large structures that are symmetrical about the equator and how the complexity of
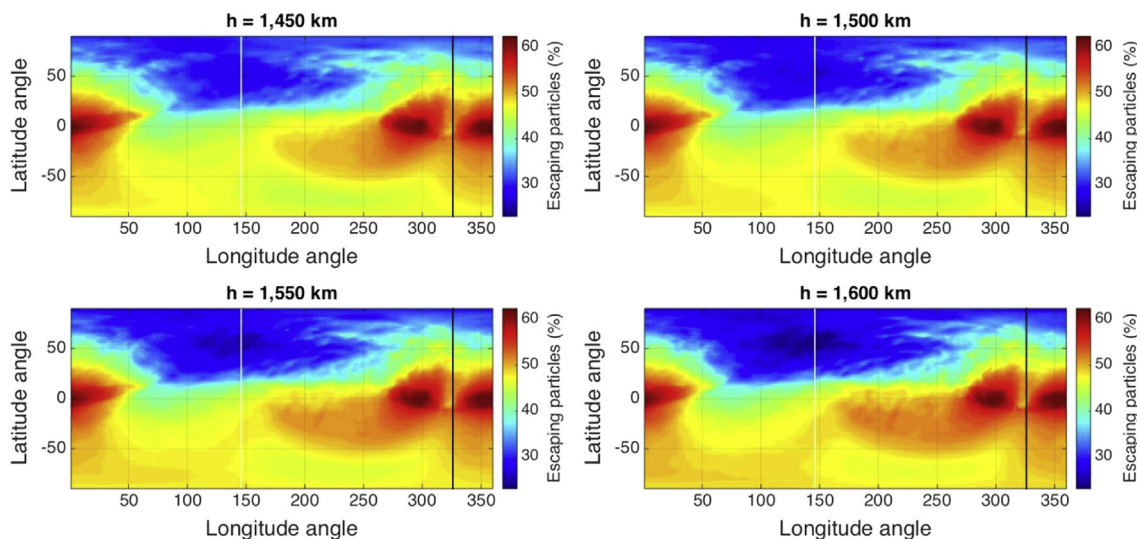
Fig. A1. Access of 1 keV O$^+$ ions to four different altitudes: 1450 km (exobase, top left), 1500 km (top right), 1550 km (bottom left) and 1600 km (bottom right).

those maps, as well as the presence of small-scale features, increases with smaller gyroradii.

Additionally, by combining data obtained from the MIMI/CHEMS instrument on-board Cassini with the access of O$^+$ and H$^+$ ions of different energies obtained using the tracing code for four different positions at the exobase of the moon, normalized fluxes were obtained that serve as an input for the calculation of ionization rates.

Finally, energy deposition and ionization rates for energetic O$^+$ and H$^+$ ions were calculated. A ratio between the maximum and minimum ionization peaks for the selected positions of approximately 18% was obtained for the case of O$^+$ ions whereas for the case of H$^+$ ions a difference of almost 80% was obtained. This means that the variations in ionization rates (and thus in ion densities) around the moon could partly be explained by the effect that the electromagnetic disturbances caused by Titan have on how magnetospheric ions are directed towards the moon and, given the importance of ionization by magnetospheric ions at the altitudes where the peaks were estimated (Figs. 16 and 17), this factor could play a major role on the local ionospheric densities.

However, in order to be able to link the results with observations made by Cassini, a more detailed study needs to be carried out including extra factors such as other atmospheric constituents (at least CH_4) as well as more complex ionization reactions. Another effect that is not considered in this study and that should play an important role is the incidence angle of the precipitating ions. This is a factor that could lead to even larger differences according to whether ions precipitate closer or farther from the vertical. This incidence angle will also be affected by the way ions are guided by the local electromagnetic fields.

Appendix A. Setting the collisionless boundary at different altitudes

By tracing back the particles using the exobase (1450 km) as a starting point and given that no particle interactions are simulated during the tracings, it is implicitly being assumed that all the environment above the exobase is collisionless. This assumption is not necessarily true and thus a further analysis including the different interactions expected according to the densities needs to be done.

To analyze the possible impact that the inclusion of these phenomena could have on the access of particles, the same simulations presented in the previous subsections were run, this time changing the altitude of the initial position with a step of 50 km on each simulation run.

The maps showing the access of 1 keV O$^+$ ions for four different altitudes (1 R_T + 1450 km, 1.2 R_T + 1450 km, 1.4 R_T + 1450 km and 1.6 R_T + 1450 km) are presented in Fig. A1, where it can be seen that still for a variation in the setting of the exobase of up to 150 km (around 5% of Titan's radius) no significant changes are present in the particle's access maps. With these results in mind, the original choice of an altitude of 1450 km for the exobase seems to be a sensible one.

References

Achilleos, N., Arridge, C.S., Bertucci, C., Jackman, C.M., Dougherty, M.K., Khurana, K. K., Russell, C.T., 2008. Large-scale dynamics of Saturn's magnetopause: observations by Cassini. J. Geophys. Res. 113 (A11209), 1–14.

Ågren, K., Wahlund, J.-E., Garnier, P., Modolo, R., Cui, J., Galand, M., Müller-Wodarg, I., 2009. On the ionospheric structure of titan. Planet. Space Sci. 57, 1821–1827 (December (14)).

Arridge, C.S., Achilleos, N., Dougherty, M.K., Khurana, K.K., Russell, C.T., 2006. Modeling the size and shape of Saturn's magnetopause with variable dynamic pressure. J. Geophys. Res. 111 (A11), 1–13.

Arridge, C.S., André, N., Bertucci, C.L., Garnier, P., Jackman, C.M., Németh, Z., Rymer, A.M., Sergis, N., Szego, K., Coates, A.J., Crary, F.J., 2011. Upstream of saturn and titan. Space Sci. Rev. 162, 25–83.

Arridge, C.S., Khurana, K.K., Russell, C.T., Southwood, D.J., Achilleos, N., Dougherty, M.K., Coates, A.J., Leinweber, H.K., 2008. Warping of Saturn's magnetospheric and magnetotail current sheets. J. Geophys. Res. 113 (A8), 1–13.

Backes, H., Neubauer, F.M., Dougherty, M.K., Achilleos, N., André, N., ArridgeC., S., Bertucci, C., Jones, G.H., Khurana, K.K., Russell, C.T., Wennmacher, A., 2005. Titan's magnetic field signature during the first cassini encounter. Science 308 (5724), 992–995.

Bertucci, C., Achilleos, N., Dougherty, M.K., Modolo, R., Coates, A.J., Szego, K., Masters, A., Ma, Y., Neubauer, F.M., Garier, P., Wahlund, J.-E., YoungD., T., 2008. The magnetic memory of titan's ionized atmosphere. Science 321 (5895), 1475–1478.

Bertucci, C., Hamilton, D.C., Kurth, W.S., Hospodarsky, G., Mitchell, D., Sergis, N., Edberg, N.J.T., Dougherty, M.K., 2015. Titan's interaction with the supersonic solar wind. Geophys. Res. Lett. 42 (2), 193–200.

Bertucci, C., Neubauer, F.M., Szego, K., Wahlund, J.E., Coates, A.J., Dougherty, M.K., Young, D.T., Kurth, W.S., 2007. Structure of Titan's mid-range magnetic tail, Cassini magnetometer observations during the T9 flyby. Geophys. Res. Lett. 34 (24), 1–4.

Bézard, B., Yelle, R.V., Nixon, C.A., 2014. The composition of Titan's atmosphere. In: Müller-Wodarg, I., Griffith, C.A., Lellouch, E., Cravens, T.E. (Eds.), Titan: Interior, Surface, Atmosphere, and Space Environment. Cambridge Planetary Science, New York.

Coates, A.J., Crary, F.J., Young, D.T., Szego, K., Arridge, C.S., Bebesi, Z., Sittler, E.C., Hartle, R.E., Hill, T.W., 2007. Ionospheric electrons in Titan's tail, plasma structure during the Cassini T9 encounter. Geophys. Res. Lett. 34 (24), 1–6.

Coates, A.J., Wellbrock, A., Lewis, G.R., Arridge, C.S., Crary, F.J., Young, D.T., Thomsen, M.F., Reisenfeld, D.B., Sittler, E.C., Johnson, R.E., Szego, K., Bebesi, Z., Jones, G.H., 2012. Cassini in Titan's tail, CAPS observations of plasma escape. J. Geophys. Res., 117.

Cravens, T.E., Robertson, I.P., Ledvina, S.A., Mitchell, D., Krimigis, S.M., Waite, J.H., 2008. Energetic ion precipitation at Titan. Geophys. Res. Lett., 35.

Cravens, T.E., Robertson, I.P., Waite, J.H., Yelle, R.V., Vuitton, V., Coates, A.J., Wahlund, J.-E., Agren, K., Richard, M.S., Haye, V.D.L., Wellbrock, A., Neubauer, F.M., 2009a. Model-data comparisons for Titan's nightside ionosphere. Icarus 199, 174–188.

Cravens, T.E., Yelle, R.V., Wahlund, J.-E., Shemansky, D.E., Nagy, A.F., 2009b. Composition and Structure of the Ionosphere and Thermosphere. In: Brown, R.H., Lebreton, J.-P., Waite, J.H. (Eds.), Titan from Cassini Huygens. Springer, Dordrecht.

Cui, J., Galand, M., Yelle, R.V., Vuitton, V., Wahlund, J.-E., Lavvas, P.P., Müller-Wodarg, I.C.F., Cravens, T.E., Kasprzak, W.T., Waite, J.H., 2009a. Diurnal variations of Titan's ionosphere. Geophys. Res, 114.

Cui, J., Yelle, R.V., Vuitton, V., Waite, J.H., Kasprzak, W.T., Gell, D.A., NiemannH., B., Müller-Wodarg, I.C.F., Borggren, N., Fletcher, G.G., Patrick, E.L., Raaen, E., Magee, B.A., 2009b. Analysis of Titan's neutral upper atmosphere from Cassini Ion Neutral Mass Spectrometer measurements. ,Icarus 200, 581–615 (April (2)).

Dialynas, K., Krimigis, S.M., Mitchell, D.G., Hamilton, D.C., Krupp, N., BrandtP., C., 2009. Energetic ion spectral characteristics in the Saturnian magnetosphere using Cassini/MIMI measurements. J. Geophys. Res. 114 (A1), 1–7.

Dougherty, M.K., Southwood, S.K.D.J., Balogh, A., Smith, E.J., Tsurutani, B.T., Gerlach, B., Glassmeier, K.-H., Gleim, F., Russell, C.T., Erdos, G., NeubauerF., M., Cowley, S. W.H., 2004. The Cassini magnetic field investigation. Space Sci. Rev. 114 (1), 331–383.

Edberg, N.J.T., Andrews, D.J., Shebanits, O., Ågren, K., Wahlund, J.-E., Opgenoorth, H. J., Roussos, E., Garnier, P., Cravens, T.E., Badman, S.V., Modolo, R., Bertucci, C., Dougherty, M.K., 2013. Extreme densities in Titan's ionosphere during the T85 magnetosheath encounter. Geophys. Res. Lett. 40 (12), 2879–2883.

Feyerabend, M., Simon, S., Motschmann, U., Saur, J., Liuzzo, L., 2015. Planet. Space Sci. 117, 362–376. http://dx.doi.org/10.1016/j.pss.2015.07.008.

Fulchignoni, M., Ferri, F., Angrilli, F., Ball, A.J., Bar Nun, A., Barucci, M.A., Bettanini, C., Bianchini, G., Borucki, W., Colombatti, G., Coradini, M., Coustenis, A., Debei, S., Falkner, P., Fanti, G., Flamini, E., Gaborit, V., Grard, R., Hamelin, M., Harri, A.M., Hathi, B., Jernej, I., Leese, M.R., Lehto, A., Stoppato, P.F.L., López-Moreno, J.J., Mäkinen, T., McDonnell, J.A.M., McKay, C.P., Molina-Cuberos, G., Neubauer, F.M., Pirronello, V., Rodrigo, R., Saggin, B., Schwingenschuh, K., Seiff, A., oes, F.S., Svedhem, H., Tokano, T., Towner, M.C., Trautner, R., Withers, P., Zarnecki, J.C., 2005. In situ measurements of the physical characteristics of Titan's environment. Nature.

Galand, M., Yelle, R., Cui, J., Wahlund, J.-E., Vuitton, V., Wellbrock, A., CoatesA., J., 2010. Ionization sources in titan's deep ionosphere. J. Geophys. Res.

Galand, M., Yelle, R.V., Coates, A.J., Backes, H., Wahlund, J.-E., 2006. Electron temperature of Titan's sunlit ionosphere. Geophys. Res. Lett. 33 (November (21)).

Garnier, P., Dandouras, I., Toublanc, D., Roelof, E.C., Brandt, P.C., Mitchell, D.G., Krimigis, S.M., Krupp, N., Hamilton, D.C., Wahlund, J.-E., 2010. Statistical analysis of the energetic ion and ENA data for the Titan environment. Planet. Space Sci. 58 (14–15), 1811–1822.

Gronoff, G., Lilensten, J., Desorgher, L., Flückiger, E., 2009. Ionization processes in the atmosphere of Titan I. Ionization in the whole atmosphere. Astron. Astrophys. 506, 955–964.

Khurana, K.K., Arridge, C.S., Schwarzl, H., Dougherty, M.K., 2006. A model of Saturn's magnetospheric field based on latest Cassini observations. In: American Geophysical Union Spring Meeting Abstracts.

Kliore, A.J., Nagy, A.F., Marouf, E.A., French, R.G., Flasar, F.M., Rappaport, N.J., Anabttawi, A., Asmar, S.W., Kahann, D.S., Barbinis, E., Goltz, G.L., Fleischman, D.U., Rochblatt, D.J., 2008. First results from the Cassini radio occultations of the Titan ionosphere. Geophys. Res. 113.

Kotova, A., Roussos, E., Krupp, N., Dandouras, I., 2015. Modeling of the energetic ion observations in the vicinity of Rhea and Dione. Icarus 258, 402–417.

Krasnopolsky, V.A., 2009. A photochemical model of Titan's atmosphere and ionosphere. Icarus 201 (1), 226–256.

Krimigis, S.M., Mitchell, D.G., Hamilton, D.C., Livi, S., Dandouras, J., Jaskulek, S., Armstrong, T.P., Boldt, J.D., Cheng, A.F., Gloeckler, G., Hayes, J.R., HsiehK., C., Ip, W.-H., Keath, E.P., Kirsch, E., Krupp, N., Lanzerotti, L.J., Lundgren, R., Mauk, B.H., McEntire, R.W., Roelof, E.C., Schlemm, C.E., Tossman, B.E., Wilken, B., Williams, D.J., 2004. Magnetosphere imaging instrument (MIMI) on the cassini mission to saturn/titan. Space Sci. Rev. 114 (1), 233–329.

Ledvina, S.A., Brecht, S.H., Cravens, T.E., 2012. The orientation of Titan's dayside ionosphere and its effects on Titan's plasma interaction. EarthPlanets Space 64 (2), 207–230.

Ledvina, S.A., Cravens, T.E., Kecskeméty, K., 2005. Ion distributions in Saturn's magnetosphere near Titan. J. Geophys. Res. 110.

Lipatov, A.S., Sittler, E.C., Hartle, R.E., Cooper, J.F., Simpson, D.G., 2014. Titan's plasma environment, 3D hybrid kinetic modeling of the TA flyby and comparison with CAPS-ELS and RPWS LP observations. Planet. Space Sci. 93–94, 119–128.

López-Moreno, J.J., Molina-Cuberos, G.J., Hamelin, M., Grard, R., oes, F.S., Godard, R., Schwingenschuh, K., Béghin, C., Berthelier, J.J., Brown, V.J.G., Falkner, P., Ferri, F., Fulchignoni, M., Jernej, I., Jerónimo, J.M., Rodrigo, R., Trautner, R., 2008. Structure of Titan's low altitude ionized layer from the Relaxation Probe onboard HUYGENS. Geophys. Res. Lett. 35 (November (22)).

Luhmann, J.G., 1996. Titan's ion exosphere wake, a natural ion mass spectrometer? J. Geophys. Res. 101, 29387–29393 (December (E12)).

Ma, Y.J., Nagy, A.F., Cravens, T.E., Sokolov, I.V., Clark, J., Hansen, K.C., 2004. 3-D Global MHD model prediction of the first close flyby of titan by cassini. Geophys. Res. Lett. 31 (22), 1–4.

Marchand, R., 2010. Test-particle simulation of space plasmas. Commun. Comput. Phys. 8 (3), 471–483.

Modolo, R., Wahlund, J.-E., Boström, R., Canu, P., Kurth, W.S., Gurnett, D., LewisG., R., Coates, A.J., 2007. Far plasma wake of titan from the RPWS observations, a case study. Geophys. Res. Lett. 34 (24), 1–6.

Molina-Cuberos, G.J., Lammer, H., Stumptner, W., Schwingenschuh, K., RuckerH., O., López-Moreno, J.J., Rodrigo, R., Tokano, T., 2001. Ionospheric layer induced by meteoric ionization in Titan's atmosphere. Planet. Space Sci. 49, 143–153 (February (2)).

Müller, J., Simon, S., Motschmann, U., Schüle, J., Glassmeier, K.-H., Pringle, G.J., 2011. A.I.K.E.F., adaptive hybrid model for space plasma simulations. Comput. Phys. Commun.

Neubauer, F.M., Backes, H., Dougherty, M.K., Wennmacher, A., Russell, C.T., Coates, A., Young, D., Achilleos, N., André, N., Arridge, C.S., Bertucci, C., Jones, G.H., Khurana, K.K., Knetter, T., Law, A., Lewis, G.R., Saur, J., 2006. Titan's near magnetotail from magnetic field and electron plasma observations and modeling, Cassini flybys TA, TB and T3. J. Geophys. Res.

Read, P.L., Dowling, T.E., Schubert, G., 2009. Saturn's rotation period from its atmospheric planetary-wave configuration. Nature 460, 608–610.

Richard, M.S., Cravens, T.E., Wylie, C., Webb, D., Chediak, Q., Mandt, K., WaiteJ., H., Rymer, A., Bertucci, C., Wellbrock, A., Windsor, A., Coates, A.J., 2015. An empirical approach to modeling ion production rates in Titan's ionosphere II, ion production rates on the nightside. Geophys. Res. Lett. 120 (2), 1281–1298.

Roederer, J.G., 1967. On the adiabatic motion of energetic particles in a model magnetosphere. J. Geophys. Res. 72 (3), 981–992.

Rymer, A.M., Smith, H.T., Wellbrock, A., Coates, A.J., Young, D.T., 2009. Discrete classification and electron energy spectra of Titan's varied magnetospheric environment. Geophys. Res. Lett., 36.

Shah, M.B., Latimer, C.J., Montenegro, E.C., Tucker, O.J., Johnson, R.E., Smith, H.T., 2009. The implantation and interactions of in Titan's atmosphere, laboratory measurements of collision-induced dissociation of and modeling of positive ion formation. Astrophys. J. 703, 1947–1954.

Sillanpää, I., 2008. Hybrid Modelling of Titan's Interaction with the Magnetosphere of Saturn. University of Helsinki (Ph.D. thesis).

Sillanpää, I., Johnson, R.E., 2015. The role of ion-neutral collisions in Titan's magnetospheric interaction, Planet. SpaceSci. 108, 73–86.

Sillanpää, I., Kallio, E., Jarvinen, R., Janhunen, P., 2007. Oxygen ions at Titan's exobase in a Voyager 1-type interaction from a hybrid simulation. J. Geophys. Res. 112 (December (A12)).

Simon, S., Kleindienst, G., Boesswetter, A., Bagdonat, T., Motschmann, U., Glassmeier, K.-H., Schuele, J., Bertucci, C., Dougherty, M.K., 2007. Hybrid simulation of Titan's magnetic field signature during the Cassini T9 flyby. Geophys. Res. Lett. 34 (24), 1–5.

Sittler, E.C., Hartle, R.E., Bertucci, C., Coates, A., Cravens, T., Dandouras, I., Shemansky, D., 2009. Energy deposition processes in Titan's upper atmosphere and its induced magnetosphere. In: Brown, R.H., Lebreton, J.-P., Waite, J.H. (Eds.), Titan from Cassini Huygens. Springer, Dordrecht.

Sittler, E.C., Hartle, R.E., Johnson, R.E., Cooper, J.F., Lipatov, A.S., Bertucci, C., Coates, A.J., Szego, K., Shappirio, M., Simpson, D.G., Wahlund, J.-E., 2010. Saturn's magnetospheric interaction with Titan as defined by Cassini encounters T9 and T18: new results. Planet. Space Sci. 58, 327–350.

Snowden, D., Winglee, R., Bertucci, C., Dougherty, M.K., 2007. Three-dimensional multifluid simulation of the plasma interaction at Titan. J. Geophys. Res. 112 (A12), 1–9.

Snowden, D., Yelle, R.V., 2014. The thermal structure of Titan's upper atmosphere, II, energetics. Icarus 228, 64–77.

Szego, K., Bebesi, Z., Bertucci, C., Coates, A.J., Crary, F., Erdos, G., Hartle, R., SittlerE., C., Young, D.T., 2007. Charged particle environment of Titan during the T9 flyby. Geophys. Res. Lett. 34.

Tseng, W.-L., Ip, W.-H., Kopp, A., 2008. Exospheric heating by pickup ions at Titan. Adv. Space Res. 42, 54–60.

Vuitton, V., Yelle, R.V., McEwan, M.J., 2007. Ion chemistry and N-containing molecules in Titan's upper atmosphere. Icarus 191 (2), 722–742.

Waite, J.H., Niemann, H., Yelle, R.V., Kasprzak, W.T., Cravens, T.E., LuhmannJ., G., McNutt, R.L., Ip, W.H., Gell, D., Hay, V.D.L., Müller Wodarg, I., Magee, B., Borggren, N., L edvina, S., Fletcher, G., Walter, E., Miller, R., Scherer, S., Thorpe, R., Xu, J., Block, B., Arnett, K., 2005. Ion neutral mass spectrometer results from the first flyby of titan. Science 308, 982–986 (May (5724)).

Wei, H.Y., Russell, C.T., Dougherty, M.K., Ma, Y.J., Hansen, K.C., McAndrewsH., J., Wellbrock, A., Coates, A.J., Thomsen, M.F., Young, D.T., 2011. Unusually strong magnetic fields in Titan's ionosphere, T42 case study. Adv. Space Res. 48 (2), 314–322.

Wei, H.Y., Russell, C.T., Dougherty, M.K., Neubauer, F.M., Ma, Y.J., 2010. Upper limits on Titan's magnetic moment and implications for its interior. J. Geophys. Res.

Wulms, V., Saur, J., Strobel, D.F., Simon, S., Mitchell, D.G., 2010. Energetic neutral atoms from Titan, particle simulations in draped magnetic and electric fields. J. Geophys. Res. 115 (A6), 1–18.

Yelle, R.V., Snowden, D.S., Müller-Wodarg, I.C.F., 2014. Titan's upper atmosphere: thermal structure, dynamics, and energetics. In: Müller-Wodarg, I., Griffith, C. A., Lellouch, E., Cravens, T.E. (Eds.), Titan: Interior, Surface, Atmosphere, and Space Environment. Cambridge Planetary Science, New York.

Yelle, R.V., Strobel, D.F., Lellouch, E., Gautier, D., 1997. Engineering Models for Titan's Atmosphere. ESA SP-1177**.

Ziegler, J.F., Ziegler, M.D., Biersack, J.P., 2010. SRIM—the stopping and range of ions in matter. Nucl. Instrum. Methods Phys. Res. B 268, 1818–1823.